

METHANOL FORMATION VIA OXYGEN INSERTION CHEMISTRY IN ICES

JENNIFER B. BERGNER¹, KARIN I. ÖBERG², MAHESH RAJAPPAN²

¹Harvard University Department of Chemistry and Chemical Biology, 10 Oxford Street, Cambridge, MA 02138, USA

²Harvard-Smithsonian Center for Astrophysics, 60 Garden Street, Cambridge, MA 02138, USA

ABSTRACT

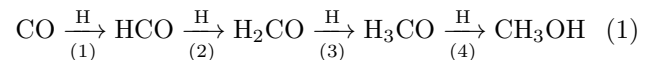
We present experimental constraints on the insertion of oxygen atoms into methane to form methanol in astrophysical ice analogs. In gas-phase and theoretical studies this process has previously been demonstrated to have a very low or non-existent energy barrier, but the energetics and mechanisms have not yet been characterized in the solid state. We use a deuterium UV lamp filtered by a sapphire window to selectively dissociate O₂ within a mixture of O₂:CH₄ and observe efficient production of CH₃OH via O(¹D) insertion. CH₃OH growth curves are fit with a kinetic model, and we observe no temperature dependence of the reaction rate constant at temperatures below the oxygen desorption temperature of 25K. Through an analysis of side products we determine the branching ratio of ice-phase oxygen insertion into CH₄: ~65% of insertions lead to CH₃OH with the remainder leading instead to H₂CO formation. There is no evidence for CH₃ or OH radical formation, indicating that the fragmentation is not an important channel and that insertions typically lead to increased chemical complexity. CH₃OH formation from O₂ and CH₄ diluted in a CO-dominated ice similarly shows no temperature dependence, consistent with expectations that insertion proceeds with a small or non-existent barrier. Oxygen insertion chemistry in ices should therefore be efficient under low-temperature ISM-like conditions, and could provide an important channel to complex organic molecule formation on grain surfaces in cold interstellar regions such as cloud cores and protoplanetary disk midplanes.

1. INTRODUCTION

Complex organic molecules (COMs) have been detected towards star-forming regions at all stages of evolution, including molecular clouds, protostellar hot cores, envelopes, and outflows, and protoplanetary disks (e.g. [Blake et al. 1987](#); [Bottinelli et al. 2004](#); [Arce et al. 2008](#); [Öberg et al. 2010, 2015](#)). It is of great interest to understand the rich chemistry that feeds the formation and destruction of these molecules in the interstellar medium (ISM) in order to constrain the chemical inventories available for pre-biotic chemistry as solar systems develop. To explain COM production, current astrochemical models typically rely on grain-surface radical recombination chemistry that becomes active in lukewarm (~30K) ices ([Garrod et al. 2008](#); [Herbst & van Dishoeck 2009](#)). However, observations of COMs towards very cold interstellar environments such as prestellar cores ([Öberg et al. 2010](#); [Bacmann et al. 2012](#); [Cernicharo et al. 2012](#), e.g.) indicate that a cold pathway to complex molecule formation must also be active.

A central challenge to building chemical complexity at low temperatures is the incorporation of several heavy elements into molecules. To address this, many experimental studies have focused on the hydrogenation of unsaturated oxygen-bearing molecules. Repeated hy-

drogenation of CO has been shown to be efficient and leads to the production of the stable molecules H₂CO and CH₃OH ([Watanabe & Kouchi 2002](#); [Fuchs et al. 2009](#)):



In addition, H atom bombardment of CO ices has been recently shown to form even more complex molecules: H atom abstractions along the CO hydrogenation pathway (1) lead to enhanced populations of radical species, which can recombine to form larger COMs ([Fedoseev et al. 2015](#); [Chuang et al. 2016](#)). However, this recombination chemistry requires diffusion of relatively heavy radical species, which in interstellar ices are not expected to be mobile at low temperatures.

Here, we present experiments demonstrating an oxygen insertion mechanism as an alternative pathway to COM formation at low temperatures, using the test case of CH₃OH formation from O insertion into CH₄. Unlike radical recombination pathways, oxygen insertion does not require diffusion of heavy species. The ability to convert hydrocarbons directly to COMs represents a novel channel to explain observed COM abundances.

The gas-phase insertion of excited O(¹D) into CH₄ has been well-studied: initially, vibrationally excited

CH₃OH is formed, and at sufficiently high pressures can be collisionally stabilized; otherwise, the molecule fragments into the radical products CH₃ + OH (DeMore & Raper 1967; Lin & DeMore 1973). In the gas phase, therefore, insertions are typically net destructive and lead to smaller rather than larger molecules. Gas-phase oxygen insertion has been shown experimentally to be essentially barrierless (e.g. DeMore & Raper 1967), and indeed theoretical studies suggest a small \sim 280K barrier (Yu & Muckerman 2004).

Oxygen insertion has also been qualitatively demonstrated in condensed systems. In Appelman et al. (1989), HOF was photolyzed within a CH₄ matrix under high vacuum (10^{-7} Torr) conditions. Parnis et al. (1993) and Lugez et al. (1994) both studied oxygen insertion into CH₄ within Ar matrices, using photolysis of N₂O and O₃ respectively for O(¹D) atom generation. Each of these studies qualitatively demonstrated CH₃OH formation via oxygen insertion in the solid state. However, to date there is no quantitative or mechanistic description of this process. Moreover, the ice compositions in these previous studies are not astrophysically realistic. In order to evaluate the extent to which oxygen insertion can lead to chemical complexity in the ISM, a detailed understanding of how this process occurs in astrophysical ice analogs is required. In particular, it is essential to determine the energetic feasibility under ISM-like conditions, and the efficiency of CH₃OH formation compared to fragmentation and other product formation.

O(¹D) atoms, which are required for this insertion process, are in the first electronically excited state with energies \sim 2eV higher than the ground state O(³P). O(¹D) production has been demonstrated by UV photolysis of a number of molecules which should be abundant in interstellar ice mantles, including O₂, CO₂, O₃, and H₂O, as well as electron impact of O₂ and CO₂ (Lee et al. 1977; Slanger & Black 1971; DeMore & Raper 1966; Stief et al. 1975; Cosby 1993; Kedzierski et al. 2013). CO₂ and H₂O are of particular importance, as H₂O is the main constituent of interstellar ices and CO₂ is typically present at abundances of \sim 10-30% with respect to H₂O (Öberg et al. 2011). Photolysis of CO₂ follows the dissociation channel to O(¹D) + CO(¹ Σ^+) between 120nm and 170nm, with measured efficiencies of 94% and 100% at 157nm and 147nm respectively (Zhu & Gordon 1990; Slanger & Black 1971). From 105nm-145nm, H₂O dissociates to H₂ + O(¹D) with an efficiency of \sim 10% (Ung 1974; Stief et al. 1975; Slanger & Black 1982). Importantly, for both CO₂ and H₂O, O(¹D) can be generated upon exposure to Lyman- α irradiation (121.6nm), which dominates the UV spectrum in cloud cores and protoplanetary disks (e.g. Öberg 2016). Therefore, dissociation of common oxygen-bearing molecules in ice mantles should produce these excited oxygen atoms, which may

then insert into neighboring hydrocarbons within the ice.

To assess the energetics and mechanism of this reaction scheme in astrophysical ice analogs, we selectively dissociate O₂ within mixed O₂:CH₄ ices and O₂:CH₄:CO ices. In Section 2, we describe the experimental apparatus and procedures. Section 3 details the data analysis techniques used, and Section 4 presents the results. In Section 5 we discuss the reaction network and mechanisms in this system, as well as the astrophysical implications of this process.

2. EXPERIMENTAL DETAILS

We use the ultra-high vacuum experiment described in detail in Lauck et al. (2015). The chamber is evacuated to a base pressure of $\sim 5 \times 10^{-10}$ Torr. A closed-cycle He cryostat cools a CsI substrate window to temperatures as low as 9K. Temperature is monitored by a temperature controller (LakeShore 335) with an estimated accuracy of 2K and a relative uncertainty of 0.1K. Ices are typically grown on the substrate by introduction of gases through a 4.8mm diameter dosing pipe at 0.7 inches from the substrate. For co-deposition experiments, two separate dosing pipes at \sim 1.2 inches from the substrate were used to introduce gases. Experiments were performed using the following gases: CH₄ (99.9% purity, Aldrich), ¹³CH₄ (99%, Aldrich), CD₄ (99%, Aldrich), ¹⁶O₂ (99.98%, Aldrich), ¹⁸O₂ (97%, Aldrich), Ar (99.95%, Aldrich), and CO (99.95%, Aldrich). To obtain mixtures, gases were combined in a differentially pumped gas line with a base pressure \sim 10⁻⁴ Torr. A Fourier transform infrared spectrometer (Bruker Vertex 70v) in transmission mode was used to measure infrared-active molecules in the ice. A quadrupole mass spectrometer (Pfeiffer QMG 220M1) continuously monitored the gas-phase species present in the chamber.

To selectively dissociate O₂ within a CH₄:O₂ mixture, we irradiate the ice samples with a H₂D₂ lamp (Hamamatsu L11798) filtered by a 0.08" thick sapphire window (MPF Products, Inc.) Figure 1a shows the spectral distribution of the UV lamp overlaid with the transmittance spectrum of sapphire with a similar thickness¹ and the UV absorption cross-sections for both CH₄ and O₂ (Cruz-Diaz et al. 2014b). The convolution of lamp intensity, sapphire transmittance, and absorption cross-section for each species is shown as the "effective" cross-section in Figure 1b. This represents the relative absorption of each molecule under the irradiation conditions of the present experiment. The absorption of CH₄ is negligible due to the cutoff of the sapphire window, while O₂

¹ <http://resources.montanainstruments.com/help/window-materials>

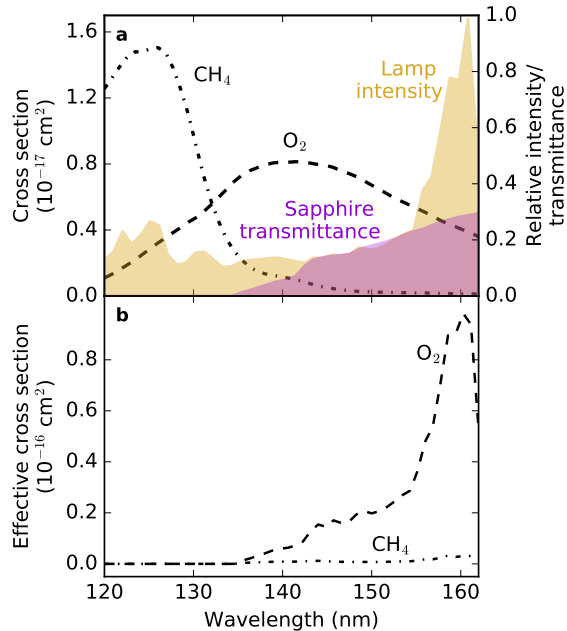


Figure 1. a: CH_4 (black dash-dot) and O_2 (black dash) UV absorption cross-sections (Cruz-Diaz et al. 2014b) overlaid with the H_2D_2 UV lamp output spectrum (gold) and sapphire transmittance spectrum (purple). b: The effective absorption cross-sections for CH_4 and O_2 resulting from the convolution of each absorption cross-section with the relative lamp intensity and window transmittance spectra.

still has a large absorption profile which is dominated by the 160.8nm Lyman band of the H_2D_2 lamp. The

photoproducts of O_2 in this wavelength regime are well-characterized: upon exposure to light at wavelengths from 140-175nm, O_2 dissociates into $\text{O}(^3\text{P}) + \text{O}(^1\text{D})$ with an efficiency of unity (Lee et al. 1977).

All experimental details are summarized in Table 1. We define different groups of experiments, each varying with respect to the Fiducial category as indicated: (I-Fiducial) $^{16}\text{O}_2:^{13}\text{CH}_4 \sim 1.4:1$, 50ML total ice thickness; (II) 20ML thickness; (III) $\sim 0.2:1$ ratio; (IV) capping layer of argon; (V) 90ML thickness; (VI): $^{12}\text{CD}_4:^{18}\text{O}_2$; (VII) other isotopologues (qualitative analysis only); (VIII) $\text{CO}:^{13}\text{CH}_4:^{16}\text{O}_2$ 4:1:1, 125ML thickness; (IX): $\text{CO}:^{13}\text{CH}_4:^{16}\text{O}_2$ 7:1:1, 170ML thickness; (X): control experiments- only 1 reactant.

The experimental procedure for groups I-VII involved a single deposition of a mixture of CH_4 and O_2 ; for groups VIII and IX, separate dosing tubes were used to co-deposit CO and a $\text{CH}_4:\text{O}_2$ mixture. In all cases, dosing was performed at 9K, followed by a 2 hour sample irradiation at a set temperature at an angle of 45° by the H_2D_2 lamp. During irradiation, IR scans were taken every 3 minutes. Following irradiation, a temperature programmed desorption (TPD) was performed by ramping the sample temperature at a rate of 2K/min to 200K. During the temperature ramp, IR scans were taken every 2 minutes and desorbing species were monitored with the QMS.

Table 1. Experiment summary

Experiment	Group	Irradiation temp (K)	Ice composition	Ratio	Total thickness (ML)
1	I	9	$^{16}\text{O}_2 : ^{13}\text{CH}_4$	1.3 : 1	53
2	I	9	$^{16}\text{O}_2 : ^{13}\text{CH}_4$	1.8 : 1	52
3	I	14	$^{16}\text{O}_2 : ^{13}\text{CH}_4$	1.4 : 1	53
4	I	19	$^{16}\text{O}_2 : ^{13}\text{CH}_4$	1.3 : 1	51
5	I	24	$^{16}\text{O}_2 : ^{13}\text{CH}_4$	1.4 : 1	50
6	I	25	$^{16}\text{O}_2 : ^{13}\text{CH}_4$	1.4 : 1	54
7	II	9	$^{16}\text{O}_2 : ^{13}\text{CH}_4$	0.9 : 1	18
8	II	14	$^{16}\text{O}_2 : ^{13}\text{CH}_4$	1.6 : 1	23
9	II	19	$^{16}\text{O}_2 : ^{13}\text{CH}_4$	1.3 : 1	19
10	III	9	$^{16}\text{O}_2 : ^{13}\text{CH}_4$	0.2 : 1	26
11	III	19	$^{16}\text{O}_2 : ^{13}\text{CH}_4$	0.2 : 1	23
12	III	24	$^{16}\text{O}_2 : ^{13}\text{CH}_4$	0.2 : 1	23
13 ^a	IV	9	$^{16}\text{O}_2 : ^{13}\text{CH}_4$	1.2 : 1	38
14	V	9	$^{16}\text{O}_2 : ^{13}\text{CH}_4$	1.6 : 1	92
15	V	9	$^{16}\text{O}_2 : ^{13}\text{CH}_4$	1.6 : 1	87
16 ^a	VI	9	$^{18}\text{O}_2 : ^{12}\text{CD}_4$	1.5 : 1	37
17	VI	9	$^{18}\text{O}_2 : ^{12}\text{CD}_4$	1.9 : 1	66
18	VI	19	$^{18}\text{O}_2 : ^{12}\text{CD}_4$	1.7 : 1	59

Table 1 continued

Table 1 (*continued*)

Experiment	Group	Irradiation temp (K)	Ice composition	Ratio	Total thickness (ML)
19 ^a	VII	9	¹⁸ O ₂ : ¹³ CH ₄	0.8 : 1	32
20	VII	9	¹⁶ O ₂ : ¹² CH ₄	1.5 : 1	55
21	VIII	9	¹² CO : ¹⁶ O ₂ : ¹³ CH ₄	4.3 : 1.1 : 1	125
22	VIII	19	¹² CO : ¹⁶ O ₂ : ¹³ CH ₄	4.5 : 1.1 : 1	127
23	VIII	19	¹² CO : ¹⁶ O ₂ : ¹³ CH ₄	4.4 : 1.1 : 1	125
24	IX	9	¹² CO : ¹⁶ O ₂ : ¹³ CH ₄	6.9 : 1.0 : 1	172
25	IX	14	¹² CO : ¹⁶ O ₂ : ¹³ CH ₄	6.8 : 1.0 : 1	172
26	IX	19	¹² CO : ¹⁶ O ₂ : ¹³ CH ₄	7.0 : 1.0 : 1	174
27	X	9	¹³ CH ₄	-	15
28	X	9	¹⁶ O ₂	-	23

^awith Ar top layer

See text for Group designations

3. DATA ANALYSIS

3.1. O₂ thickness determination

Since O₂ is infrared inactive, we quantify the O₂ dose by calibrating the time-integrated QMS signal to the IR-determined CH₄ dose as in [Fayolle et al. \(2013\)](#):

$$N_{O_2} = N_{CH_4} \frac{\int I_{O_2^+} dt}{\int I_{CH_4^+} dt} \frac{\sigma_{CH_4^+}}{\sigma_{O_2^+}}. \quad (2)$$

Here, N_x is the column density of species x , $\int I_x dt$ is the time-integrated QMS intensity of each molecule's dominant ion, and σ_x is the gas-phase electron impact ionization cross-section of each molecular ion at 70eV. The QMS mass signals m/z 17, 20, 32, and 36 are used to trace ¹³CH₄, CD₄, ¹⁶O₂, and ¹⁸O₂ respectively; these masses should not be contaminated by signal from any other molecule. O₂ and CH₄ cross-sections are taken from [Straub et al. \(1996\)](#) and [Straub et al. \(1997\)](#) respectively. The average value of $N_{CH_4} / \int I_{CH_4^+} dt$ from all experiments was used to convert to O₂ doses; based on variations between experiments, we expect an O₂ dose uncertainty of about 30%. The CH₄ thickness uncertainty is ~20%, arising mainly due to the uncertainty in band strength.

3.2. UV flux

The photon flux from the UV lamp was measured with a NIST calibrated AXUV-100G photo-diode at the sample holder to be $\sim 1.4 \times 10^{13}$ photons cm⁻² s⁻¹, with a measurement uncertainty of ~5% for the wavelengths of interest in this work. For a 2-hour irradiation, this results in a total fluence of 1×10^{17} cm⁻². To ensure that UV photons penetrate the entire ice sample, we calculate the attenuation of photons for experiments of

different ice thickness. The photon attenuation is calculated at 160.8nm, since this represents the peak of the “effective” cross-section (Section 2), using the formula

$$N_X = -\frac{1}{\sigma_X(\lambda)} \ln \frac{I_t(\lambda)}{I_0(\lambda)} \quad (3)$$

where N_X is the column density of molecule X (molecule cm⁻²), $\sigma_X(\lambda)$ is the UV absorption cross-section, and $I_t(\lambda)$ and $I_0(\lambda)$ are the transmitted and incident intensities, respectively. We assume the standard monolayer coverage of 10^{15} molecules cm⁻² and cross-sections $\sigma_{O_2}(160.8\text{nm}) = 3.9 \times 10^{-18}$ cm² and $\sigma_{CO}(160.8\text{nm}) = 0.9 \times 10^{-18}$ cm² ([Cruz-Diaz et al. 2014a,b](#)). For O₂ ice, 15, 35, and 65ML will absorb 6%, 13%, and 22% of photons respectively. For CO ice, 85 and 135ML will absorb 7% and 11% of photons respectively. Therefore, photon attenuation is small and should not impact the experimental results even for the thickest O₂ and CO ices.

3.3. IR spectra and growth curves

IR spectra were used to determine the initial ice column densities of CH₄ as well as the growth of products during irradiation. Each spectrum is averaged over 128 interferograms and takes approximately 2 minutes to complete. Column densities of each species were calculated using the integrated area of IR features:

$$N_i = \frac{2.3 \int \tau_i(\nu) d\nu}{A_i}, \quad (4)$$

where N_i is column density (molecule cm⁻²), $\int \tau_i(\nu) d\nu$ is the integrated area of the IR band (absorbance units), and A_i is the band strength in optical depth units. The standard monolayer coverage of 10^{15} molecules cm⁻² was assumed.

Table 2. IR band strengths

Molecule	Mode	Line center (cm ⁻¹)		A (cm molec ⁻¹)
		(¹³ C/ ¹⁶ O/H)	(¹² C/ ¹⁸ O/D)	
CH ₄	ν_4 bend	1291	989	8.4 x 10 ⁻¹⁸ (a)
CH ₃ OH	ν_8 CO str	1008	952	1.8 x 10 ⁻¹⁷ (a)
O ₃	ν_3 a-str	1034	975	8.8 x 10 ⁻¹⁸ (b)
CO	str	2092		1.1 x 10 ⁻¹⁷ (a)
CO ₂	ν_3 a-str	2276		1.3 x 10 ⁻¹⁶ (a)
H ₂ CO	ν_2 CO str	1683		9.6 x 10 ⁻¹⁸ (a)
	ν_3 CH ₂ sc.	1498		3.9 x 10 ⁻¹⁸ (a)
H ₂ O	ν_2 bend	1652		1.1 x 10 ⁻¹⁷ (a)

^aBouilloud et al. (2015)

^bLoeffler et al. (2006); re-scaled from RAIRS value

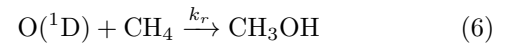
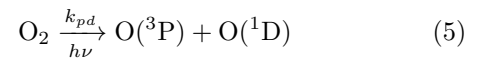
Product growth curves can only be measured for ¹³CH₄:¹⁶O₂ and ¹²CD₄:¹⁸O₂ mixtures (Groups I-VI and VIII-IX), as other isotopologue combinations have overlapping O₃ and CH₃OH infrared features. IR band centers and strengths used for quantifying molecule abundances are listed in Table 2.

O₃ column densities are highly uncertain since only RAIRS band strengths were available in the literature. However, absolute O₃ measurements are not required for quantifying the reaction between O atoms and CH₄. To estimate the ozone abundance, we assume that the ratio between RAIRS and transmission band strengths is consistent within an experiment (e.g. Ioppolo et al. 2008). We therefore scale the RAIRS band strength of O₃ reported in Loeffler et al. (2006) by the ratio of the transmission and RAIRS band strengths for the H₂O ν_2 bending mode (~ 1.4 ; Bouilloud et al. 2015; Loeffler et al. 2006).

For CH₃OH, the direct product of O insertion into CH₄, the strongest feature is the ν_8 band. Due to the proximity of the O₃ ν_3 band, both features were fit simultaneously with Gaussian profiles. Each feature is well-fit by a double Gaussian; thus, for each spectrum we fit four Gaussians as seen in Figure 2a. Fitting is done using the python *emcee* package (Foreman-Mackey et al. 2013). In addition to the four Gaussian profiles, we simultaneously fit a local linear baseline term as part of the overall fit. This enables us to incorporate any uncertainties that arise from the choice of baseline into subsequent analysis. Figure 9 in Appendix A shows an example corner plot displaying the degree of parameter covariance as well as the fit convergence.

3.4. Kinetic modeling

The reaction steps leading to methanol formation are:



where k_{pd} is the photodissociation rate of O₂ and k_r is the rate of oxygen insertion to form methanol. In addition to formation via O insertion, CH₃OH can also be photo-dissociated by UV light in this wavelength range. To account for potential CH₃OH loss we include a destruction term in the kinetic model:



As detailed in previous work, there are numerous possible products of CH₃OH processing (Bennett et al. 2007; Öberg et al. 2009). For the purposes of fitting growth curves, we are mainly interested in the loss of CH₃OH, and discuss the potential formation of other products in more detail in Section 4. We note that CH₃OH could also be consumed by other mechanisms such as H abstractions, however we assume that photodissociation is the dominant destruction mechanism. Incorporating other pathways would require modeling the entire system simultaneously, which is not practical given difficulties in measuring column densities of each product throughout the experiment.

From Reactions 6 and 7 we obtain the integrated rate law describing CH₃OH formation:

$$[\text{CH}_3\text{OH}](t) = \frac{k_r N_{ss} (e^{-k_{dest}t} - e^{-k_r t})}{k_r - k_{dest}} \quad (8)$$

where N_{ss} is a proportionality factor representing the steady-state abundance. We have assumed that the timescales of O(¹D) atom formation and destruction are much faster than the reaction timescale, and therefore

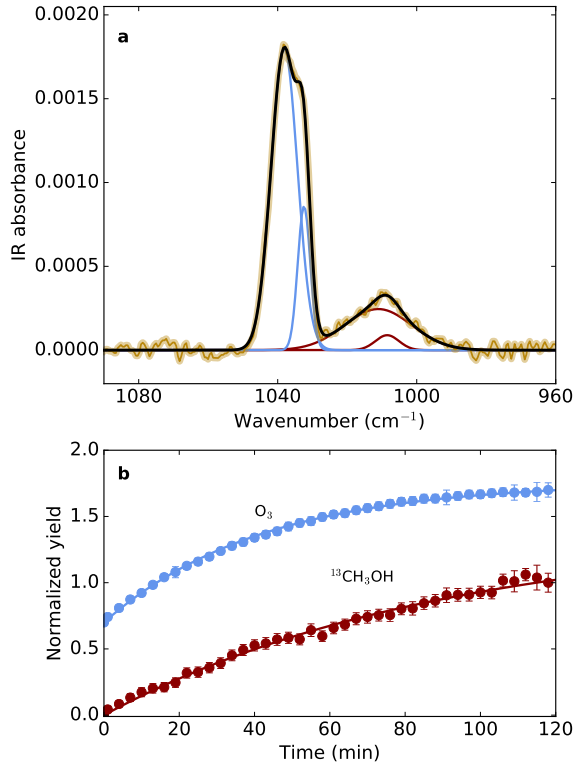


Figure 2. a: Example fit to infrared bands of O_3 at 1034cm^{-1} and $^{13}\text{CH}_3\text{OH}$ at 1008cm^{-1} . The experimental spectrum is shown in gold and the total fit in black, with individual Gaussians in blue for ozone and red for methanol. b: Scatter points show experimental growth curves for O_3 (blue; offset) and $^{13}\text{CH}_3\text{OH}$ (red). Kinetic fits are shown as solid lines. Both panels show results from Experiment 3. Product yield has been normalized by the column density at the end of 2 hours of irradiation.

the photodissociation kinetics of O_2 (Reaction 5) do not contribute to the overall growth rate. Indeed, typical CH_3OH formation rates are on the order of 10^{-4}ML s^{-1} , while the timescale for O formation ($\sim \sigma_{O_2} \times \text{flux} \times N_{O_2}$) is an order of magnitude faster, and the rate constant for $O(^1D)$ relaxation to $O(^3P)$ in solids is on the order of $\sim 1\text{ s}^{-1}$ (Mohammed 1990).

For fitting Equation 8 to growth curves, we assume that the rate constant for photodestruction of CH_3OH is equal to that of photon absorption, or $\sigma_{\text{CH}_3\text{OH}} \times \text{flux}$. $\sigma_{\text{CH}_3\text{OH}}$ is taken from Cruz-Diaz et al. (2014a) to be $2.9 \times 10^{-18}\text{ cm}^2$ at 160.8nm for a total absorption rate = $4.1 \times 10^{-5}\text{ s}^{-1} = k_{dest}$. An example fit is shown in Figure 2b for $^{13}\text{CH}_3\text{OH}$ and O_3 growth curves during the irradiation of a $^{13}\text{CH}_4:^{16}\text{O}_2$ ice mixture (Experiment 3). The fits are very good, indicating that this model is indeed appropriate and that no additional parameters are required to describe the kinetics. Growth curves along with best-fit kinetic models for all other experiments are shown in Appendix B.

4. RESULTS

4.1. Proof of concept: CH_3OH production

During irradiation of $^{13}\text{CH}_4:^{16}\text{O}_2$ mixtures, $^{13}\text{CH}_3\text{OH}$ formation is observed in situ by the growth of the infrared band at 1008 cm^{-1} . Figure 3a shows this feature in the spectrum of pure $^{13}\text{CH}_3\text{OH}$. The band is not formed during irradiation of pure $^{13}\text{CH}_4$ or pure $^{16}\text{O}_2$, but does grow during irradiation of a mixture of $^{13}\text{CH}_4:^{16}\text{O}_2$. The growth of $^{16}\text{O}_3$ can also be seen in the pure $^{16}\text{O}_2$ and mixed $^{13}\text{CH}_4:^{16}\text{O}_2$ experiments.

Figure 3b and c show results from the TPD following sample irradiation. In Figure 3b, the QMS trace for m/z 33, which corresponds to the mass of $^{13}\text{CH}_3\text{OH}$, is observed for the mixed irradiated sample. Desorption occurs around 140K , as in the $^{13}\text{CH}_3\text{OH}$ standard. No m/z 33 signal is observed for either of the pure control experiments. Figure 3c shows the integrated IR band area around 1008cm^{-1} during the temperature ramp. Again, in the mixed irradiated experiment, the band disappears around 140K and matches well with the $^{13}\text{CH}_3\text{OH}$ standard.

Mixtures of $\text{CD}_4:^{18}\text{O}_2$ similarly demonstrated growth of $\text{CD}_3^{18}\text{OD}$. A standard was not commercially available, however we identify the band at 952cm^{-1} as $\text{CD}_3^{18}\text{OD}$ based on its similar growth to $^{13}\text{CH}_3\text{OH}$ during irradiation (Figure 3d). Furthermore, m/z 38 corresponding to $\text{CD}_3^{18}\text{OD}$ desorbs around 140K coincident with the depletion of the IR band at 952cm^{-1} (Figure 3e and f). We therefore confirm the O insertion behavior in two isotopologue systems; based on these different lines of evidence, CH_3OH is produced during the irradiation of $\text{CH}_4:\text{O}_2$ mixtures.

Table 3. CH_3OH growth curve parameter fits: $\text{CH}_4:\text{O}_2$ experiments

Expt.	N_{ss} (ML)	k_r (s^{-1})
1	3.5 [0.4]	$1.1 [0.1] \times 10^{-4}$
2	3.0 [0.5]	$1.0 [0.2] \times 10^{-4}$
3	4.9 [1.0]	$6.3 [1.3] \times 10^{-5}$
4	3.1 [0.3]	$1.2 [0.2] \times 10^{-4}$
5	3.8 [0.7]	$8.0 [1.5] \times 10^{-5}$
6	7.1 [1.8]	$4.0 [1.1] \times 10^{-5}$
7	1.5 [0.4]	$1.2 [0.3] \times 10^{-4}$
8	0.8 [0.4]	$1.5 [0.4] \times 10^{-4}$
9	1.1 [0.5]	$1.1 [0.4] \times 10^{-4}$
10	2.5 [0.6]	$7.5 [1.7] \times 10^{-5}$
11	1.2 [0.2]	$1.4 [0.3] \times 10^{-4}$
12	1.0 [0.3]	$1.6 [0.3] \times 10^{-4}$
13	2.1 [0.2]	$1.5 [0.2] \times 10^{-4}$
14	3.8 [1.3]	$9.5 [3.4] \times 10^{-5}$
15	2.8 [0.9]	$1.2 [0.4] \times 10^{-4}$

Table 3 continued

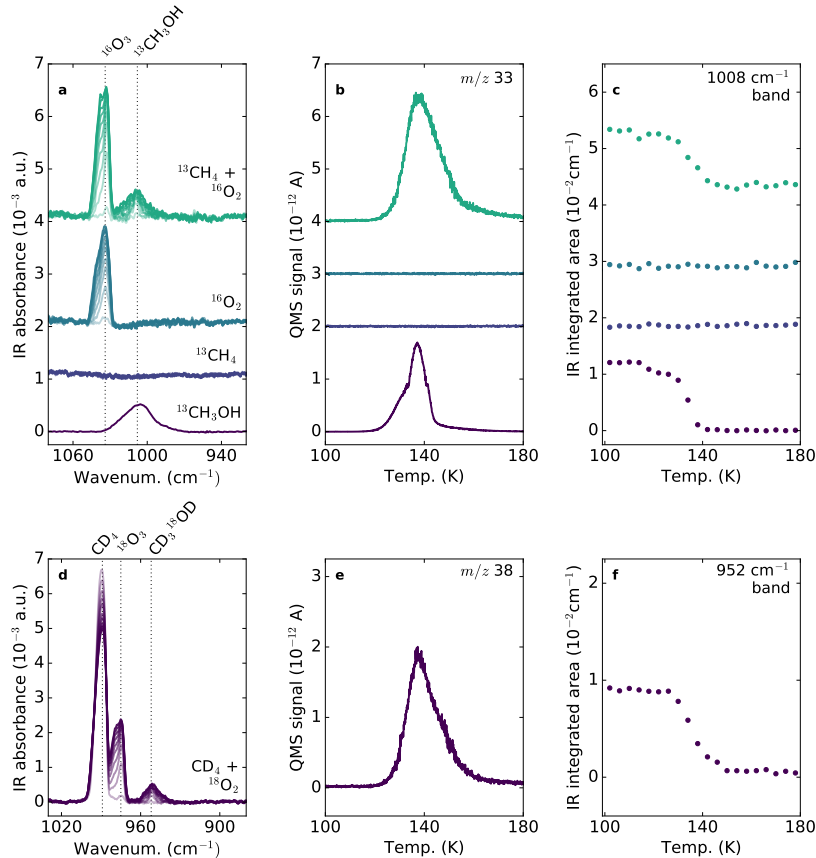


Figure 3. CH_3OH production demonstrated through growth of IR features during irradiation (a,d), QMS traces during TPD (b,e), and integrated IR bands during TPD (c,f). Top panels show results for irradiated $^{13}\text{CH}_4 + ^{16}\text{O}_2$ mixture, irradiated $^{16}\text{O}_2$ only, irradiated $^{13}\text{CH}_4$ only, and a $^{13}\text{CH}_3\text{OH}$ standard. Bottom panels show results for irradiated $\text{CD}_4 + ^{18}\text{O}_2$.

Table 3 (continued)

Expt.	N_{ss} (ML)	k_r (s^{-1})
16	3.1 [1.5]	$7.1 [3.3] \times 10^{-5}$
17	7.0 [3.3]	$3.9 [2.1] \times 10^{-5}$
18	5.7 [2.5]	$5.4 [2.4] \times 10^{-5}$

Uncertainties listed in brackets

4.2. $\text{O}_2:\text{CH}_4$ Experiments

4.2.1. Rate constants

To assess the energetics of oxygen insertion into CH_4 , experiments were performed at 9K, 14K, 19K, 24K, and 25K. As described in Section 3.3, first-order kinetic models with photodissociative loss were used to fit each growth curve. Fits are typically performed for 2 hours of irradiation, however for ices thicker than 30ML fits are performed for 1 hour irradiations since peak overlap between the CH_3OH and O_3 feature becomes more severe for the higher product column densities. The parameters k_r and N_{ss} for each model are listed in Table 3.

The scatter in rate constants from all $^{13}\text{CH}_4 + ^{16}\text{O}_2$ experiments performed at 9K was used to estimate uncertainties due to day-to-day systematics. We find a standard deviation of $\sim 20\%$ in the rate constant values; for all experiments, this systematic uncertainty was added in quadrature with the growth curve fit errors in order to obtain the final uncertainties on k_r .

Figure 4 shows Arrhenius plots of the rate constants for different groups of experiments. For all $^{13}\text{CH}_4 + ^{16}\text{O}_2$ experiments at temperatures below 25K, there is no temperature dependence to the CH_3OH formation rate constant: regardless of the ice thickness, the $\text{CH}_4:\text{O}_2$ ratio, or the presence of an inert capping gas, the value of k_r is consistent around 10^{-4}s^{-1} . The lower rate at 25K is likely due to the onset of oxygen desorption. In experiments of $\text{CD}_4 + ^{18}\text{O}_2$ the actual rate constants for $\text{CD}_3^{18}\text{OD}$ production are slightly lower than for $^{13}\text{CH}_3\text{OH}$; this could be due to deuterium exchange altering the apparent kinetics, or a difference in zero-point energy impacting the reaction rates. As for $^{13}\text{CH}_4 + ^{16}\text{O}_2$ experiments there is no temperature dependence between 9K and 19K, indicating similar underlying energetics for the different isotopologue systems. The lack

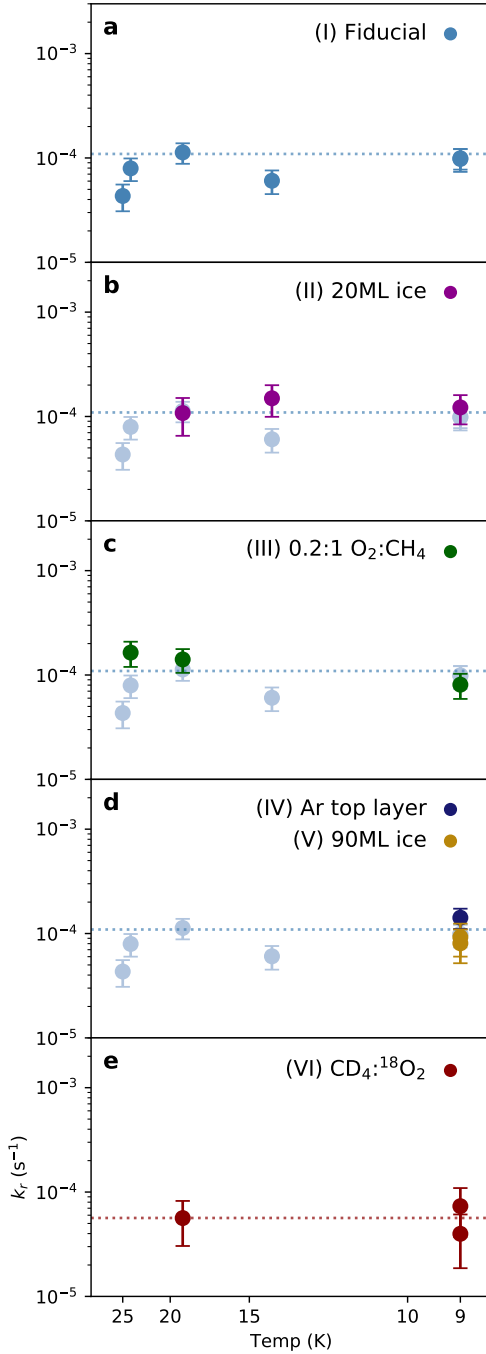


Figure 4. Arrhenius plots for CH_3OH growth. Fiducial experiments ($\sim 1.4:1$ $^{13}\text{CH}_4:^{16}\text{O}_2$, 50ML total ice thickness) are shown in the top panel and reproduced in the other $^{13}\text{CH}_4:^{16}\text{O}_2$ experiments. All other panels show experiments that differ from the fiducial group as indicated, with experimental group number shown in parentheses. Dotted blue lines (a-d) show the mean rate constant for all $^{13}\text{CH}_4:^{16}\text{O}_2$ experiments; the dotted red line (e) shows the mean rate constant for $\text{CD}_4:^{18}\text{O}_2$ experiments.

of temperature dependence on the reaction rate is consistent with expectations from gas-phase and theoretical studies, which demonstrate barrierless or almost barrierless insertion of $\text{O}(^1\text{D})$ into CH_4 .

4.2.2. Other products

O₃, H₂CO, CO, CO₂, and H₂O are formed during the irradiation in addition to CH₃OH. These are identi-

fied from their infrared features (Figure 5), which shift as predicted for different isotope combinations. IR line centers used for identification and corresponding references are listed in Table 4.

Table 4. Observed infrared line centers for isotopologue experiments

Position (cm ⁻¹)	Assignment	Reference	Position (cm ⁻¹)	Assignment	Reference
<u>¹³CH₄ + ¹⁶O₂</u>			<u>¹³CH₄ + ¹⁸O₂</u>		
3000	¹³ CH ₄	a	3000	¹³ CH ₄	a
2825	¹³ CH ₃ OH	a	2807	¹³ CH ₄	a
2807	¹³ CH ₄	a	2240	¹³ C ¹⁸ O ₂	e
2276	¹³ CO ₂	b	2039	¹³ C ¹⁸ O	f
2092	¹³ CO	b	1652	H ₂ ¹³ C ¹⁸ O	g
1683	H ₂ ¹³ CO	c*	1645	H ₂ ¹⁸ O	h*
1652	H ₂ O	b	1291	¹³ CH ₄	a
1498	H ₂ ¹³ CO	c*	979	¹⁸ O ₃	d*
1291	¹³ CH ₄	a		¹³ CH ₃ ¹⁸ OH	g
1034	O ₃	d*	<u>¹²CH₄ + ¹⁶O₂</u>		
1008	¹³ CH ₃ OH	a	3009	CH ₄	a
<u>¹²CD₄ + ¹⁸O₂</u>			2822	H ₂ CO	b
3237	CD ₄	a	2815	CH ₄	a
2306	C ¹⁸ O ₂	e	2341	CO ₂	b
2251	CD ₄	a	2139	CO	b
2088	C ¹⁸ O	f	1718	H ₂ CO	b
1631	D ₂ C ¹⁸ O	g	1659	H ₂ O	b
989	CD ₄	a	1495	H ₂ CO	b
975	O ₃	d*	1300	CH ₄	a
952	CD ₃ ¹⁸ OD	g	1033	O ₃	d*
				CH ₃ OH	b

*Original assignment in RAIRS

^aReference spectrum in this work; ^bBouilloud et al. (2015); ^cKaiser et al. (2015); ^dSchriver-Mazzuoli et al. (1995); ^eDu et al. (2011); ^fLegay-Sommaire & Legay (1982); ^gAssigned based on shifts from other isotopologues; ^hZheng et al. (2011)

None of the isotopologue combinations result in clean IR features for all products. For unblended features in the ¹³CH₄:¹⁶O₂ experiments, growth curves can be measured from integrated IR spectra using the band strengths listed in Table 2. An example set of growth curves is shown in Figure 6. CH₄ is steadily consumed over the course of the experiment; CH₃OH and H₂CO growth begins at early times, while CO₂ growth accelerates later in the irradiation.

Final yields of all products are calculated from the IR spectrum after 2 hours of irradiation. For products with

blended features, yields are estimated as follows. The CO band is blended in ¹³CH₄:¹⁶O₂ experiments, but not for ¹³CH₄:¹⁸O₂ and ¹²CH₄:¹⁶O₂ (Exps. 19 and 20). In both unblended cases the ratio of CO/CO₂ is equal to ~1.3. Therefore, the CO yield in ¹³CH₄:¹⁶O₂ experiments is estimated by multiplying the CO₂ yield by 1.3. H₂O overlaps with the H₂CO feature at 1683cm⁻¹. To estimate the H₂O yield, the H₂CO contribution is calculated based on the area of its 1498cm⁻¹ feature and then subtracted from the integrated area of the entire blended feature.

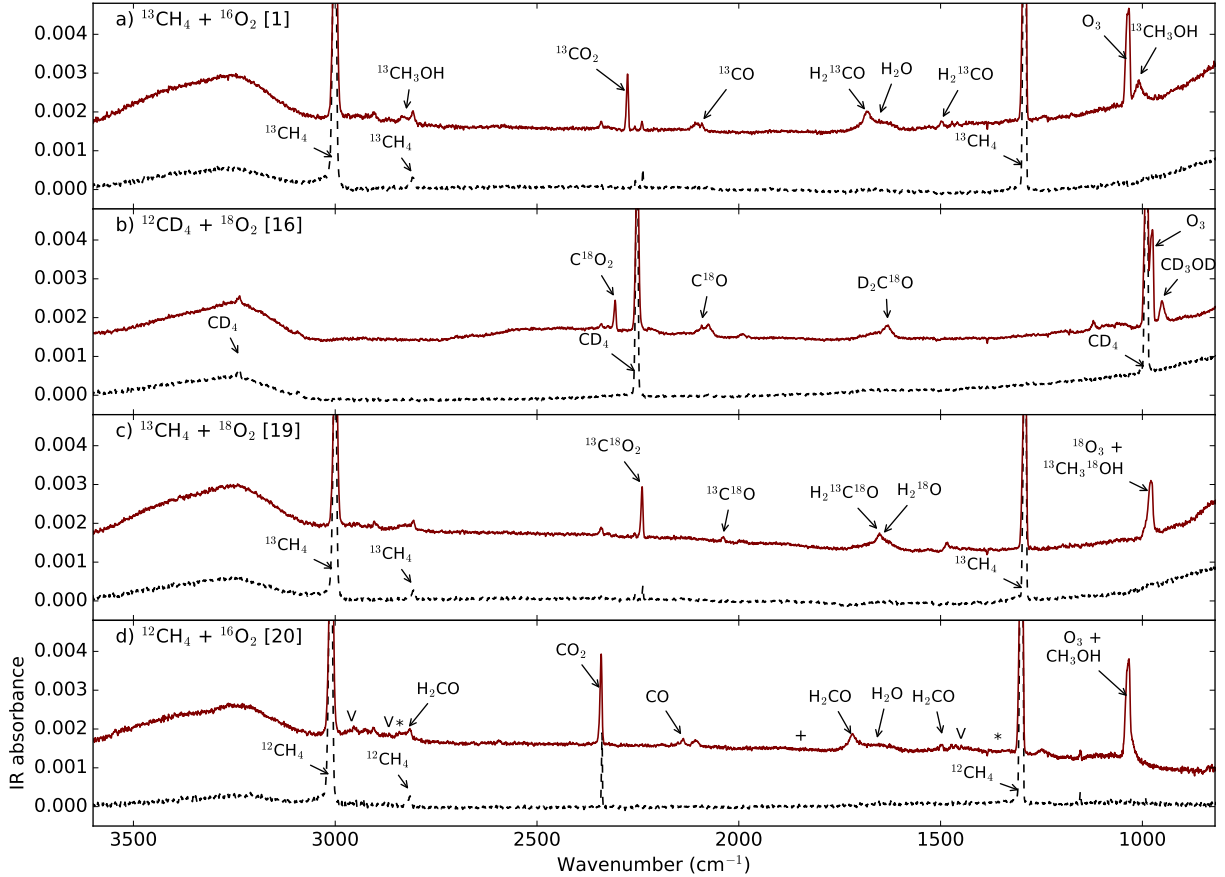


Figure 5. $\text{CH}_4 + \text{O}_2$ ice mixtures before (black dashed line) and after (red solid line) 2h UV irradiation, with reactant and product IR peaks labeled. Each panel shows a different isotope combination, with the experiment number indicated in brackets. In the $^{12}\text{CH}_4:^{16}\text{O}_2$ experiment (d), line centers for H_2O_2 , C_2H_6 , and HCO are shown with *'s, V's, and +'s respectively.

Table 5. Average product yields after 2h irradiation

CO	CO ₂	H ₂ CO	CH ₃ OH	H ₂ O	O ₃
(% wrt CH ₄ consumed)				(% wrt O ₂ dose)	
6.8 [0.6]	5.3 [0.5]	26.3 [8.7]	60.0 [6.2]	11.8 [4.5]	12.7 [1.4]

Standard deviations listed in brackets

Average product yields (Table 5) are calculated from experiments in Groups I, IV, and V, which all have sufficiently large IR features for all molecules to be quantified. Total yields of carbon-bearing products are consistent with the measured consumption of CH_4 when considering band strength uncertainties.

4.2.3. Branching ratio

The ratios of carbon-bearing products can be used to derive the branching ratio of $\text{O}(^1\text{D}) + \text{CH}_4 \rightarrow \text{CH}_3\text{OH}$. As seen in Table 5, CH_3OH has an average yield of $60 \pm 6\%$ with respect to CH_4 consumption. This represents a lower limit to the CH_3OH formation efficiency

since, as described in Section 3.4, CH_3OH is also susceptible to photodissociation. We can calculate the maximum abundance of carbon-bearing derivatives that may be formed from CH_3OH photoprocessing using the integrated rate law for product formation by Reaction 7:

$$[\text{pr}](t) = \frac{N_{\text{ss}}[k_{\text{dest}}(1 - e^{-k_r t}) - k_r(1 - e^{-k_{\text{dest}} t})]}{k_{\text{dest}} - k_r}, \quad (9)$$

where $[\text{pr}]$ represents the combined abundance of products from CH_3OH destruction. This represents an upper limit on the actual amount of products formed since not every photon absorption is necessarily dissociative. Us-

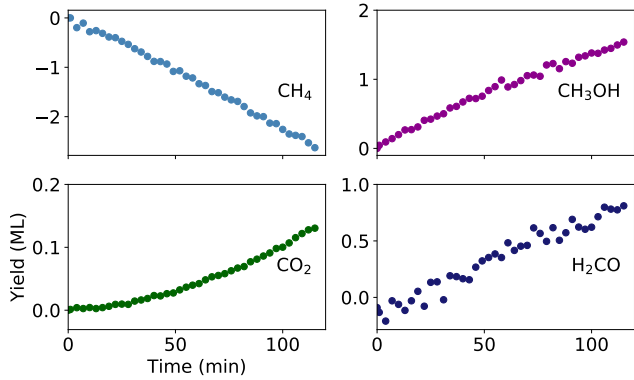


Figure 6. Growth curves in a $^{13}\text{CH}_4\text{:}^{16}\text{O}_2$ experiment (Exp. 3) for molecules with unblended IR features: CH_4 (ν_4 bend), CH_3OH (ν_8 CO str), CO_2 (ν_3 a-str), and H_2CO (ν_3 CH_2 sc).

ing the values of k_r and N_{ss} derived from fitting CH_3OH growth curves (Table 3), we find an average upper limit of $9.7 \pm 1\%$ photo-products with respect to CH_4 consumption after 2 hours.

Assuming that CO and CO_2 are daughter species of H_2CO processing, the summed abundance of CO, CO_2 , and H_2CO represents the total number of H_2CO molecules that are formed over the course of an experiment. Experimentally, the average total abundance of $\text{H}_2\text{CO} + \text{CO} + \text{CO}_2$ is equal to $38 \pm 9\%$ with respect to CH_4 consumption. Therefore, we observe more carbon-bearing side products than can be produced purely through CH_3OH photoprocessing. The remaining products are likely formed from the product channel $\text{O}(^1\text{D}) + \text{CH}_4 \rightarrow \text{H}_2\text{CO} + \text{H}_2$. The branching ratio of this channel should be equal to the difference between the observed side products and calculated abundances of photo-products. This value will represent a lower limit since the calculated photoproduct yield is based on the assumption that every photon absorbed by CH_3OH is dissociative. We obtain a lower limit for the H_2CO channel branching ratio of $29 \pm 9\%$. Based on this analysis we can therefore bracket the branching ratio of the CH_3OH channel between $\sim 60\text{--}71\%$, with the lower limit representing a scenario with no CH_3OH photodissociation and the upper limit representing the maximum possible CH_3OH photodissociation.

Performing this same treatment at other time points, we find that the mean H_2CO branching ratio begins small and increases over the irradiation, flattening out to 28-29% after 90 minutes. This is consistent with a scenario in which some H_2CO comes directly from O insertion, and some from CH_3OH dissociation.

We note that an abstraction pathway of $\text{O} + \text{CH}_4 \rightarrow \text{OH} + \text{CH}_3$ is a negligible or non-existent channel: if important, there should be considerable amounts of C_2H_6 and H_2O_2 from $\text{CH}_3 + \text{CH}_3$ and $\text{OH} + \text{OH}$, and we do not detect C_2H_6 or H_2O_2 as products. We deter-

mine upper limits for each species using Experiment 20 ($^{12}\text{CH}_4\text{:}^{16}\text{O}_2$), as band strengths and positions are most reliable for the standard isotopes. The line centers where H_2O_2 and C_2H_6 should appear are shown in Figure 5d; qualitatively, it is clear that these are minor species if they are present at all. To determine the C_2H_6 upper limit, we use the ν_{10} band at 2972cm^{-1} ($2.2 \times 10^{-17}\text{cm molec}^{-1}$; Hudson et al. 2014). We find an upper limit of 0.05ML, or $\sim 1.7\%$ with respect to CH_4 consumption. Only RAIRS band strengths are available in the literature for H_2O_2 and so, as for described for O_3 in Section 3.3, we scale the RAIRS band strength reported in Loeffler et al. (2006). For the ν_6 bending mode at 1368cm^{-1} this yields a band strength of $3.0 \times 10^{-17}\text{cm molec}^{-1}$. We find an H_2O_2 upper limit of 0.01ML, compared to a typical O_3 yield of $\sim 4\text{ML}$ for experiments with similar initial doses. Thus, these species are either not produced or are a small fraction of the total reaction.

4.3. CO dilution experiments

In order to evaluate whether CH_3OH formation via $\text{O}(^1\text{D})$ insertion into CH_4 is also efficient in a more astrophysically realistic environment, we performed a set of experiments (21-26) in which the reactants $^{16}\text{O}_2$ and $^{13}\text{CH}_4$ were diluted in ^{12}CO . CO absorbs UV radiation, thereby introducing the possibility of contamination from CO-induced chemistry. However, by following the formation of ^{12}C vs. ^{13}C products we determine that ^{12}CO mainly reacts to form $^{12}\text{CO}_2$. We follow the growth of $^{13}\text{CH}_3\text{OH}$ in order to determine the oxygen insertion kinetics.

Table 6. CH_3OH growth curve parameter fits: CO: O_2 : CH_4 experiments

Expt.	N_{ss} (ML)	k_r (s^{-1})
21	0.54 [0.15]	$1.1 [0.3] \times 10^{-4}$
22	0.70 [0.33]	$5.1 [2.6] \times 10^{-5}$
23	0.38 [0.15]	$9.8 [3.9] \times 10^{-5}$
24	1.43 [0.90]	$1.6 [1.3] \times 10^{-5}$
25	0.54 [0.45]	$3.7 [3.1] \times 10^{-5}$
26	0.55 [0.46]	$3.5 [3.1] \times 10^{-5}$

Uncertainties listed in brackets

Rate constants for CH_3OH formation are determined by fitting Equation 8 as before. CH_3OH formation rate constants are derived at temperatures between 9K-19K for ices of two different compositions: 4:1:1 $^{12}\text{CO}:^{16}\text{O}_2:^{13}\text{CH}_4$ mixtures and 7:1:1 $^{12}\text{CO}:^{16}\text{O}_2:^{13}\text{CH}_4$ mixtures. Since product yields are reduced when the reactants are diluted in CO, uncertainties on the rate

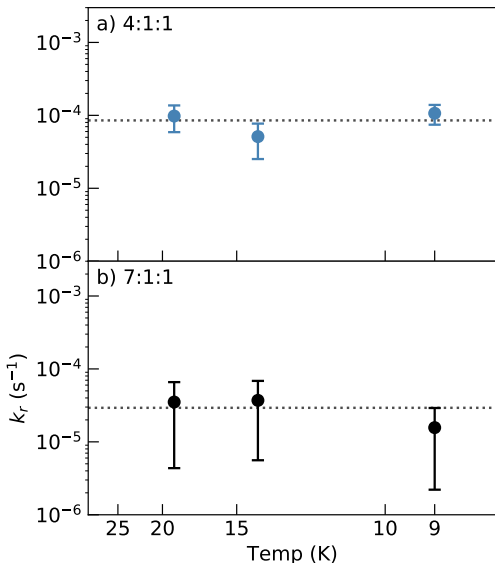


Figure 7. Rate constants as a function of temperature for CO dilution experiments. a) 4:1:1 $^{12}\text{CO}:^{16}\text{O}_2:^{13}\text{CH}_4$. b) 7:1:1 $^{12}\text{CO}:^{16}\text{O}_2:^{13}\text{CH}_4$.

constants are higher than in the $\text{O}_2:\text{CH}_4$ experiments. Still, as can be seen from the Arrhenius plots (Figure 7), there is no temperature dependence to the CH_3OH formation rate. The parameters k_r and N_{ss} are shown in Table 6.

5. DISCUSSION

5.1. Reaction network

As mentioned in Section 1, for the UV wavelengths in this study, O_2 dissociation proceeds through the channel $\text{O}_2 \rightarrow \text{O}(^1\text{D}) + \text{O}(^3\text{P})$ with an efficiency of unity (Lee et al. 1977). Thus, our ices should contain equal parts $\text{O}(^1\text{D})$ and $\text{O}(^3\text{P})$. We now draw from gas-phase, theoretical, and, when available, condensed-phase studies to interpret the formation pathways of our observed products. Figure 8 presents a summary of the possible pathways we discuss.

CH_3OH formation: In the gas phase the insertion of $\text{O}(^1\text{D})$ into CH_4 results in an excited CH_3OH product, which undergoes unimolecular dissociation to form mainly $\text{OH} + \text{CH}_3$ unless it is stabilized by e.g. collision (DeMore & Raper 1967; Parnis et al. 1993) or supersonic expansion (Hays et al. 2015). As our experiments involve condensed ices, it is fully consistent that the intact CH_3OH molecule is observed due to energy dissipation into the solid. This insertion process has been demonstrated to have essentially no barrier in gas-phase and theoretical studies (DeMore & Raper 1967; Yu & Muckerman 2004), which is again consistent with the lack of a temperature dependence to CH_3OH formation in our experiments.

In contrast, ground state $\text{O}(^3\text{P})$ oxygen atoms follow

an abstraction channel with CH_4 to produce $\text{OH} + \text{CH}_3$, with an estimated barrier of over 5000K (e.g. Walch & Dunning Jr. 1980; Zhao et al. 2016). Such an abstraction channel could conceivably lead to CH_3OH production through radical recombination, however this is unlikely due to the high theoretical energy barrier. Furthermore, as stated in Section 4.2.3, the upper limits for C_2H_6 and H_2O_2 are on the order of a percent or less of the total consumed CH_4 , indicating that abstraction is not an important process in this system.

O_3 formation: O_3 formation from energetic processing of molecular oxygen under astrochemically relevant conditions has been well-described in the literature (e.g. Schriver-Mazzuoli et al. 1995; Bennett & Kaiser 2005; Sivaraman et al. 2011). The mechanism for O_3 formation under these conditions is $\text{O}(^3\text{P}) + \text{O}_2$. This is likely the formation pathway occurring in our ices as well since $\text{O}(^3\text{P})$ should be formed in similar quantities as $\text{O}(^1\text{D})$, and the barrier to react with CH_4 , the other available reaction partner, is high.

H_2CO formation: A fraction of H_2CO may be formed from photo-processing of CH_3OH , as has been demonstrated in previous UV irradiation studies (e.g. Gerakines et al. 1996; Öberg et al. 2009). As discussed in Section 4.2.3, the majority of H_2CO is likely formed directly from insertion of $\text{O}(^1\text{D})$ into CH_4 . Indeed, following CH_3OH , H_2CO is the next most stable possible product of $\text{O}(^1\text{D})$ insertion into CH_4 (Chang & Lin 2002; Yu & Muckerman 2004), and gas-phase and matrix studies typically show H_2CO as the second-most common insertion product (e.g. DeMore & Raper 1967; Appelman et al. 1989; Hays et al. 2015). Moreover, from Figure 6 the shape of the H_2CO growth curve is different from the second-generation product CO_2 , but quite similar to that of the primary insertion product CH_3OH . This is consistent with a scenario in which the majority of H_2CO forms from the same mechanism as CH_3OH , as opposed to growing only from CH_3OH processing.

CO formation: Successive H abstractions could form CO via $\text{H}_2\text{CO} \rightarrow \text{HCO} \rightarrow \text{CO}$, but as seen in Figure 5d HCO is not observed in the IR despite having a comparable band strength to CO (Bennett et al. 2007). Alternatively, CO may be produced by unimolecular dissociation of H_2CO to directly form $\text{CO} + \text{H}_2$, which is a demonstrated photo-process of H_2CO in the condensed phase (Thomas Jr. & Guillory 1973) and explains the lack of observed HCO .

H_2O formation: Hydrogenation channels beginning with O , O_2 , or O_3 have been shown experimentally to lead to water formation (Dulieu et al. 2010; Ioppolo et al. 2008; Romanzin et al. 2011) and are likely at play in this system given the availability of these reactants. An alternative pathway is the formation and subsequent hydrogenation of OH by the abstraction pathway of $\text{O}(^3\text{P})$

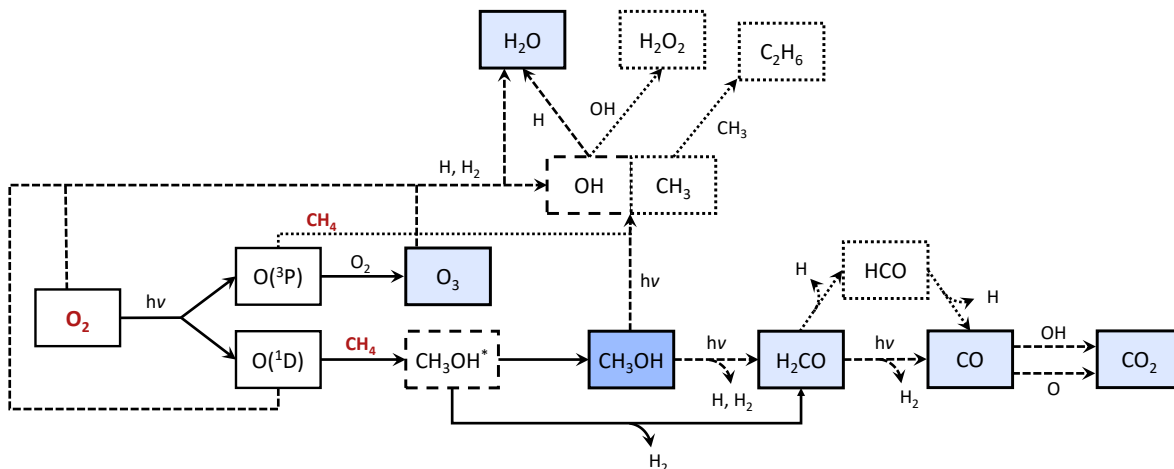


Figure 8. Proposed network for this reaction system. Reactants are shown with red text, and observed products as blue boxes. Boxes with dashed borders indicate intermediates that are likely based on observed products; dotted borders indicate intermediates/products that are not observed and therefore minor channels if present at all. Solid lines represent pathways leading to primary products; dashed lines represent pathways leading to secondary products; dotted lines represent pathways that are likely minor contributions based on the lack of observed products.

with CH_4 . However, given the high barrier to the $O(^3P)$ abstraction pathway and lack of observed C_2H_6 , reaction pathways beginning with O , O_2 , or O_3 are more likely.

CO₂ formation: From the shape of its growth curve (Figure 6), CO_2 is almost certainly a second-generation product, with its abundance increasing at later times in the experiment. One possible route for CO_2 formation is $CO + OH$, with OH formed as an intermediate along the H_2O formation channels. Studies have also shown CO_2 formation from $CO + O$ (Parnis et al. 1993; Madzunkov et al. 2006; Minissale et al. 2013). It is unclear whether the higher energy barrier of the $CO + O$ pathway or the higher diffusion barrier of the $CO + OH$ pathway will dominate under these conditions.

5.2. *O* insertion reaction

We derive a branching ratio for the CH_3OH channel of $\sim 65\%$, with the remaining insertions leading to H_2CO formation. Fragmentation does not appear to be an important process in this system as evidenced by the lack of CH_3 and OH chemistry. Solid-state oxygen insertions should therefore lead to a net increase in chemical complexity, in most cases increasing the size of the product molecule and in all cases forming an O-containing organic from a hydrocarbon.

We observe no temperature dependence to CH_3OH formation via oxygen insertion, consistent with gas-phase and theoretical studies which show a negligible or non-existent energy barrier. With these experiments alone, however, we cannot definitively rule out the presence of a small energy barrier for several reasons. First, our experiments cannot isolate any contributions from tunneling, which may play a role at the low tempera-

tures studied here. Additionally, it is possible that a diffusion barrier for O atoms could mask an insertion barrier, since the atoms would have to overcome a barrier to diffuse away than to react. Based on rather low diffusion barriers for O atoms in models ($\sim 400K$; Garrod & Pauly 2011), only a small reaction barrier could be masked in this way. Finally, the photodissociation of O_2 may lead to the formation of “hot” oxygen atoms: the threshold for formation of $O(^3P) + O(^1D)$ is 175nm (Nee & Lee 1997), whereas the UV lamp in this study peaks at 160.8nm. This energy difference represents $\sim 0.6eV$. Some of this excess energy will be dissipated into the solid, but it is possible that oxygen atoms formed as a result of photodissociation are superthermal.

A hot atom mechanism may also be at play in ISM ices: as described in Section 1, the $O(^1D)$ required for oxygen insertion chemistry in astrophysical settings is likely formed from photolysis or radiolysis of oxygen-bearing molecules. The possibility that oxygen insertion is driven by hot atoms in our experiments makes it important to explore in ices with more realistic compositions than $O_2:CH_4$ mixtures. In the CO -dominated experiments (Section 4.3), we found that even when the reactants are diluted in a CO ice, the CH_3OH formation rate follows the same temperature-independent trend as in the $O_2:CH_4$ only experiments. Thus, whether $O(^1D)$ insertion is mediated by a hot atom mechanism or not, we find that it can proceed at very low temperatures in a barrierless/pseudo-barrierless manner.

When taken along with the theoretical insertion barrier of just $\sim 280K$ and a negligible measured insertion barrier in the gas phase, an essentially barrierless ice-phase insertion process is the most likely explanation

for our experimental results. We conclude that insertion is a dominant reaction pathway when excited $O(^1D)$ is present, and furthermore that it proceeds pseudo-barrierlessly in ISM-like ices.

5.3. Astrophysical implications

In the interstellar medium, O insertion pathways could be of particular importance in very cold regions where radical diffusion chemistry is not thermally accessible. Indeed, gas-phase chemistry leading to hydrocarbon formation is known to be very efficient at low temperatures; these hydrocarbons can then accrete onto grain surfaces. Meanwhile, as mentioned in Section 1, excited $O(^1D)$ atoms can be formed by energetic processing of common oxygen-bearing constituents of astrophysical ices (in particular, H_2O and CO_2). The insertion of oxygen atoms directly into hydrocarbons would then lead to the formation of a variety of complex organic species, without the need for radical diffusion. The degree to which this type of chemistry contributes to COM formation will need to be tested by astrochemical modelers. In this case, it will be important to distinguish between $O(^3P)$ and $O(^1D)$ atoms in order to accurately account for the chemistry.

Ultimately it will be important to quantify the process of O insertion into larger hydrocarbons: CH_3OH , while a convenient test case, can be produced in astrochemical models via CO hydrogenation. Larger organics, on the other hand, are regularly underproduced in models and therefore seemingly missing a formation pathway. From the limited literature available, O insertions into both saturated and unsaturated larger hydrocarbons should occur at low temperatures in condensed phases (Parnis et al. 1993; DeMore 1969), though further experiments are required to quantify the energetics and product distribution of such systems. While we expect to see a low or non-existent insertion barrier for larger hydrocarbons, it is important to obtain branching ratios for the insertion products: the C-H bonds are not necessarily degenerate in larger hydrocarbons as they are in CH_4 , making it difficult to predict a priori which products will form. Moreover, gas-phase studies suggest that an abstraction channel becomes increasingly competitive with insertion for larger hydrocarbons (Luntz 1980). There is also some evidence for O insertion into C-C bonds in the gas phase (Yang 2006). The experimental setup used in this study cannot be used to test oxygen insertions into other hydrocarbons, as most larger hydrocarbons have appreciable UV absorption cross-sections above the sapphire window cutoff; however, testing these systems experimentally should be possible with an atomic beam setup. Quantitative constraints on the energetics and product distributions of O atom insertion into larger hydrocarbons will enable an evaluation of the impor-

tance of oxygen insertion chemistry to forming complex molecules in astrophysical environments.

6. CONCLUSIONS

We have experimentally tested and quantified the formation of CH_3OH via oxygen insertion into methane in astrophysical ice analogs. From our results we conclude:

1. Selective dissociation of O_2 in mixed $O_2:CH_4$ ices results in the formation of CH_3OH in various isotopologue studies. The growth kinetics of CH_3OH are well described by a model that includes both formation and photo-dissociative loss.
2. A direct insertion mechanism of $O(^1D)$ atoms into CH_4 explains CH_3OH formation, with a minor channel of H_2CO production and no evidence of fragmentation to $CH_3 + OH$. $O(^1D)$ insertions in ices therefore lead to a net increase in chemical complexity. We quantify the steady-state branching ratio to CH_3OH to be 60-71%.
3. Experiments with varying ice thicknesses and reactant ratios show no temperature dependence to the CH_3OH formation rate constant k_r from 9-24K. This holds even when the reactants are diluted in a CO matrix, consistent with a small or non-existent energy barrier to insertion.
4. Experimental constraints on the energetics and branching ratios of O insertions into larger hydrocarbons are required to assess the contribution of oxygen insertion chemistry to observed abundances of COMs.

The authors thank Edith Fayolle, Robin Garrod, and Ilsa Cooke for valuable feedback. J.B.B acknowledges funding from the National Science Foundation Graduate Research Fellowship under Grant DGE1144152. K.I.O. acknowledges funding from the Simons Collaboration on the Origins of Life (SCOL) investigator award.

Software: emcee (Foreman-Mackey et al. 2013)

7. APPENDIX A: IR SPECTRUM FITTING WITH MCMC

For $^{16}O_2:^{13}CH_4$ experiments, each IR spectrum was fit from $940-1090cm^{-1}$. The scan immediately prior to irradiation was subtracted from each irradiation spectrum. Irradiation spectra were then fit with a model consisting of a linear baseline term and four Gaussians:

$$y(x) = y_o + m(x - x_o) + a_1 e^{-(x-b_1)^2/2c_1^2} + a_2 e^{-(x-b_2)^2/2c_2^2} + a_3 e^{-(x-b_3)^2/2c_3^2} + a_4 e^{-(x-b_4)^2/2c_4^2}, \quad (10)$$

where y_o and x_o represent the y and x offsets for the baseline, a_n are the Gaussian amplitudes, b_n are the Gaussian centers, and c_n are the Gaussian widths. An example corner plot from MCMC fitting with *emcee* is shown in Figure 9; for clarity, the fit parameters for two Gaussians are shown rather than all 16 parameters simultaneously. For fitting the $^{18}\text{O}_2:\text{CD}_4$ experiments, the wavelength range used for fitting was $900\text{-}965\text{cm}^{-1}$, and only two Gaussians were required in the model since the $^{18}\text{O}_3$ feature is sufficiently well-separated from $\text{CD}_3^{18}\text{OD}$. For $\text{CO}:^{16}\text{O}_2:^{13}\text{CH}_4$ experiments, spectra were fit from $980\text{-}1030\text{cm}^{-1}$ and due to low product yields a single Gaussian was sufficient to fit the CH_3OH feature.

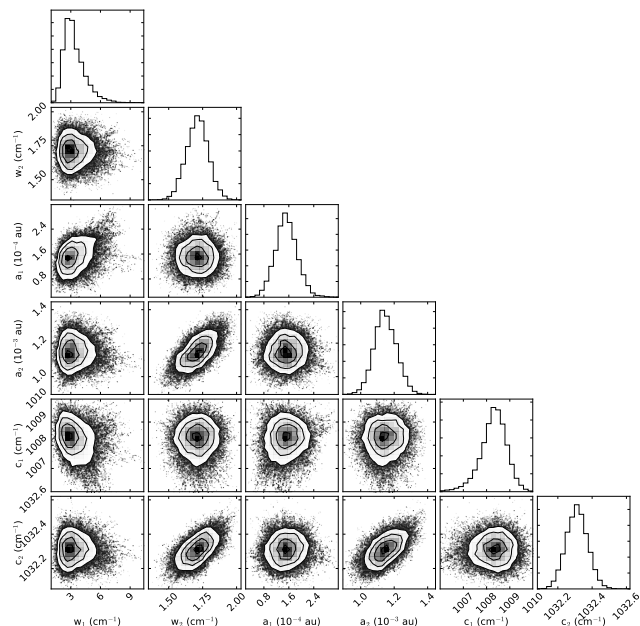


Figure 9. Example corner plot showing the covariance of two Gaussians used to fit the spectrum shown in Figure 2a.

8. APPENDIX B: EXPERIMENTAL GROWTH CURVES AND MODEL FITS

Growth curves along with best-fit kinetic models for all experiments are shown in Figure 10.

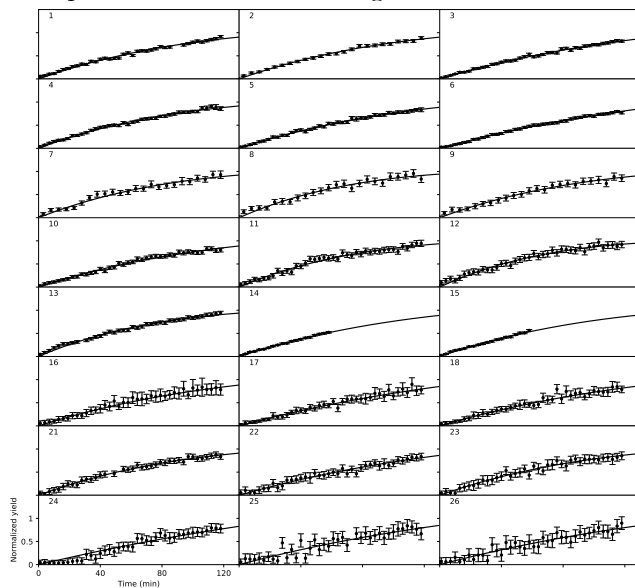


Figure 10. Experimental growth curves with best-fit kinetic models for all experiments. Experiment numbers from Table 1 are listed in each subplot.

REFERENCES

Appelman, E. H., Downs, A. J., & Gardner, C. J. 1989, *JPhCh*, 93, 598

Arce, H. G., Santiago-García, J., Jørgensen, J. K., Tafalla, M., & Bachiller, R. 2008, *ApJL*, 681, L21

- Bacmann, A., Taquet, V., Faure, A., Kahane, C., & Ceccarelli, C. 2012, *A&A*, 541, L12
- Bennett, C. J., Chen, S.-H., Sun, B.-J., Chang, A. H. H., & Kaiser, R. I. 2007, *ApJ*, 660, 1588
- Bennett, C. J., & Kaiser, R. I. 2005, *ApJ*, 635, 1362
- Blake, G. A., Sutton, E. C., Masson, C. R., & Phillips, T. G. 1987, *ApJ*, 315, 621
- Bottinelli, S., Ceccarelli, C., Lefloch, B., et al. 2004, *ApJ*, 615, 354
- Bouilloud, M., Fray, N., Bénilan, Y., et al. 2015, *MNRAS*, 451, 2145
- Cernicharo, J., Marcelino, N., Roueff, E., et al. 2012, *ApJL*, 759, L43
- Chang, A. H. H., & Lin, S. H. 2002, *CPL*, 363, 175
- Chuang, K.-J., Fedoseev, G., Ioppolo, S., van Dishoeck, E. F., & Linnartz, H. 2016, *MNRAS*, 455, 1702
- Cosby, P. C. 1993, *JChPh*, 98, 9560
- Cruz-Diaz, G. A., Muñoz Caro, G. M., Chen, Y.-J., & Yih, T.-S. 2014a, *A&A*, 562, A119
- Cruz-Diaz, G. A., Muñoz Caro, G. M., Chen, Y.-J., & Yih, T.-S. 2014b, *A&A*, 562, A120
- DeMore, W. B. 1969, *JPhCh*, 73, 391
- DeMore, W. B., & Raper, O. F. 1966, *JChPh*, 44, 1780
- DeMore, W. B., & Raper, O. F. 1967, *JChPh*, 46, 2500
- Du, J., Wan, L., Wu, L., et al. 2011, *JPCA*, 115, 1040
- Dulieu, F., Amiaud, L., Congiu, E., et al. 2010, *A&A*, 512, A30
- Fayolle, E. C., Bertin, M., Romanzin, C., et al. 2013, *A&A*, 556, A122
- Fedoseev, G., Cuppen, H. M., Ioppolo, S., Lamberts, T., & Linnartz, H. 2015, *MNRAS*, 448, 1288
- Foreman-Mackey, D., Hogg, D. W., Lang, D., & Goodman, J. 2013, *PASP*, 125, 306
- Fuchs, G. W., Cuppen, H. M., Ioppolo, S., et al. 2009, *A&A*, 505, 629
- Garrod, R. T., Widicus Weaver, S. L., & Herbst, E. 2008, *ApJ*, 682, 283
- Garrod, R. T., & Pauly, T. 2011, *ApJ*, 735, 15
- Gerakines, P. A., Schutte, W. A., & Ehrenfreund, P. 1996, *A&A*, 312, 289
- Hays, B. M., Wehres, N., DePrince, B. A., et al. 2015, *CPL*, 630, 18
- Herbst, E., & van Dishoeck, E. F. 2009, *ARA&A*, 47, 427
- Hudson, R. L., Gerakines, P. A., & Moore, M. H. 2014, *Icar*, 243, 148
- Ioppolo, S., Cuppen, H. M., Romanzin, C., van Dishoeck, E. F., & Linnartz, H. 2008, *ApJ*, 686, 1474
- Kaiser, R. I., Maity, S. J., & Jones, B. M. 2015, *Angewandte Chemie*, 127, 197
- Kedzierski, W., Hein, J. D., Tiessen, C. J., et al. 2013, *Can. J. Phys.*, 91, 1044
- Lauck, T., Karssemeijer, L., Shulenberger, K., et al. 2015, *ApJ*, 801, 118
- Lee, L. C., Slanger, T. G., Black, G., & Sharpless, R. 1977, *JChPh*, 67, 5602
- Legay-Sommaire, N., & Legay, F. 1982, *CP*, 66, 315
- Lin, C. L., & DeMore, W. B. 1973, *JPhCh*, 77, 863
- Loeffler, M. J., Teolis, B. D., & Baragiola, R. A. 2006, *JChPh*, 124, 104702
- Luntz, A. C. 1980, *JChPh*, 73, 1143
- Lugez, C., Schriver, A., Levant, R., & Schriver-Mazzouli, L. 1994, *CP*, 181, 129
- Madzunkov, S., Shortt, B. J., MacAskill, J. A., Darrach, M. R., & Chutjian, A. 2006, *PhRvA*, 73, 020901
- Minissale, M., Congiu, E., Manicò, G., Pirronello, V., & Dulieu, F. 2013, *A&A*, 559, A49
- Mohammed, H. H. 1990, *JChPh*, 93, 412
- Nee, J. B., & Lee, P. C. 1997, *JPCA*, 101, 6653
- Öberg, K. I. 2016, *ChRv*, 116(17), 9631
- Öberg, K. I., Boogert, A. C. A., Pontoppidan, K. M., et al. 2011, *ApJ*, 740, 109
- Öberg, K. I., Bottinelli, S., Jørgensen, J. K., & van Dishoeck, E. F. 2010, *ApJ*, 716, 825
- Öberg, K. I., Garrod, R. T., van Dishoeck, E. F., & Linnartz, H. 2009, *A&A*, 504, 891
- Öberg, K. I., Guzmán, V. V., Furuya, K., et al. 2015, *Nature*, 520, 198
- Parnis, J. M., Hoover, L. E., Fridgen, T. D., & Lafleur, R. D. 1993, *JPhCh*, 97, 10708
- Romanzin, C., Ioppolo, S., Cuppen, H. M., van Dishoeck, E. F., & Linnartz, H. 2011, *JChPh*, 134, 084504
- Schriver-Mazzouli, L., de Saxc, A., Lugez, C., Camy-Peyret, C., & Schriver, A. 1995, *JChPh*, 102, 690
- Sivaraman, B., Mebel, A. M., Mason, N. J., Babikov, D., & Kaiser, R. I. 2011, *PCCP*, 13, 421
- Slanger, T. G., & Black, G. 1971, *JChPh*, 54, 1889
- Slanger, T. G., & Black, G. 1982, *JChPh*, 77, 2432
- Stief, L. J., Payne, W. A., & Klemm, R. B. 1975, *JChPh*, 62, 4000
- Straub, H. C., Renault, P., Lindsay, B. G., Smith, K. A., & Stebbings, R. F. 1996, *PhRvA*, 54, 2146
- Straub, H. C., Lin, D., Lindsay, B. G., Smith, K. A., & Stebbings, R. F. 1997, *JChPh* 106, 4430
- Thomas Jr., S. G., & Guillory, W. A. 1973, *JPhCh*, 77, 2469
- Ung, A. Y. M. 1974, *CPL*, 28, 603
- Walch, S. P., & Dunning Jr., T. H. 1980, *JChPh*, 72, 3221
- Watanabe, N., & Kouchi, A. 2002, *ApJL*, 571, L173
- Yang, X. 2006, *PCCP*, 8, 205
- Yu, H., & Muckerman, J. T. 2004, *JPCA*, 108, 8615
- Zhao, H., Wang, W., & Zhao, Y. 2016, *JPCA*, 120, 7589
- Zheng, W., Kim, Y. S., & Kaiser, R. I. 2011, *PCCP*, 13, 15749
- Zhu, Y. F., & Gordon, R. J. 1990, *JChPh*, 92, 2897